Skin dose mapping for fluoroscopically guided interventions

Perry B. Johnson and David Borrego
Biomedical Engineering, University of Florida, Gainesville, Florida 32611

Stephen Balter
Radiology, Columbia University Medical Center, New York, New York 10032

Kevin Johnson
Radiology, University of Florida, Jacksonville, Florida 32209

Daniel Siragusa
Radiology, Division of Vascular Interventional Radiology, University of Florida, Jacksonville, Florida 32209

Wesley E. Bolch[a)]
Biomedical Engineering, University of Florida, Gainesville, Florida 32611

(Received 3 May 2011; revised 24 June 2011; accepted for publication 15 August 2011; published 19 September 2011)

Purpose: To introduce a new skin dose mapping software system for interventional fluoroscopy dose assessment and to analyze the benefits and limitations of patient-phantom matching.
Methods: In this study, a new software system was developed for visualizing patient skin dose during interventional fluoroscopy procedures. The system works by translating the reference point air kerma to the location of the patient's skin, which is represented by a computational model. In order to orient the model with the x-ray source, geometric parameters found within the radiation dose structured report (RDSR) are used along with a limited number of in-clinic measurements. The output of the system is a visual indication of skin dose mapped onto an anthropomorphic model at a resolution of 5 mm. In order to determine if patient-dependent and patient-sculpted models increase accuracy, peak skin dose was calculated for each of 26 patient-specific models and compared with doses calculated using an elliptical stylized model, a reference hybrid model, a matched patient-dependent model and one patient-sculpted model. Results were analyzed in terms of a percent difference using the doses calculated using the patient-specific model as the true standard.
Results: Anthropometric matching, including the use of both patient-dependent and patient-sculpted phantoms, was shown most beneficial for left lateral and anterior–posterior projections. In these cases, the percent difference using a reference model was between 8 and 20%, using a patient-dependent model between 7 and 15%, and using a patient-sculpted model between 3 and 7%. Under the table tube configurations produced errors less than 5% in most situations due to the flattening affects of the table and pad, and the fact that table height is the main determination of source-to-skin distance for these configurations. In addition to these results, several skin dose maps were produced and a prototype display system was placed on the in-clinic monitor of an interventional fluoroscopy system.
Conclusions: The skin dose mapping program developed in this work represents a new tool that, as the RDSR becomes available through automated export or real-time streaming, can provide the interventional physician information needed to modify behavior when clinically appropriate. The program is nonproprietary and transferable, and also functions independent to the software systems already installed on the control room workstation. The next step will be clinical implementation where the workflow will be optimized along with further analysis of real-time capabilities. © *2011 American Association of Physicists in Medicine*. [DOI: 10.1118/1.3633935]

Key words: fluoroscopically guided interventions, skin dose, radiation dose structured reports, hybrid phantoms, skin dosimetry

I. INTRODUCTION

In February 2011, the National Council on Radiation Protection and Measurement (NCRP) released its Report No. 168.[1] This comprehensive document includes 31 recommendations of which no less than ten relate to patient dose monitoring and documentation. The significance of these recommendations highlights one of the primary concerns of the interventional physician—the management of radiological risk and specifically the management of radiation induced skin injury. The effects of radiation damage to the skin can range from transient erythema and epilation to severe dermal atrophy, induration, and ulceration with the latter often requiring surgical intervention. Considerable effort has been devoted toward the prevention of such injuries through intensive training of residents, the development of dose reducing imaging systems and an overall increase in physician awareness. While these efforts have reduced the incidence of injury, any damage that does

occur is almost always unanticipated, yet in many cases is avoidable had prior knowledge of peak skin dose and approaching thresholds been available.[2] Due to the current lack of automated skin dose monitoring, this type of information is being denied to the physician who must then rely on indirect dose metrics and indicators along with their clinical experience to manage patient risk. Additionally, The Joint Commission has specifically identified skin burns caused by prolonged fluoroscopy greater than 15 Gy as a sentinel event requiring root cause analysis and a comprehensive response.[3] Currently, a large burden is placed on clinical staffing to reconstruct skin dose when a sentinel event is thought to have occurred. In effect, a team must be assembled to play the role of detective by interviewing the performing physician to determine details from the individual examination. They must then try to piece together the limited amount of information found in the patient's medical record and stored images.[4,5] The lack of automated skin dose monitoring in the clinic thus limits both the quality of patient care and the efficiency of the interventional unit for designing better safeguards.

During the past several years, a number of changes have occurred which greatly increase the prospects for the automated monitoring of patient skin dose. The first such change has been the widespread adoption of the reference point air kerma, $K_{a,r}$, which was first proposed in 2000 by the International Electrotechnical Commission (IEC) and later adopted as a regulation in 2005 by the U.S. Food and Drug Administration (FDA).[6,7] The intent was to provide a better way to estimate air kerma at the level of the patient's skin. The point of calculation is defined at a position 15 cm from the isocenter (x-ray tube side) along the central axis of the C-arm. The air kerma at this location can be provided in a number of ways depending on the vendor. Some manufacturers provided the reference point air kerma using internal look-up tables based on exposure parameters. If the fluoroscope is equipped with a air kerma-area product (P_{KA} or KAP) meter, the reference point air kerma is sometimes measured directly by dividing out the field size at the reference location. A third method employs a dual chamber (measuring both $K_{a,r}$ and P_{KA}) in the head of the machine to determine a central axis dose, which is then projected to the reference location. Regardless of the method used, the result is an estimate of the air kerma at a point 15 cm from the isocenter which moves with the gantry and traces the contour of a cylindrical phantom having a diameter of 30 cm. Due to the fact that the contour will differ from that of a real patient, $K_{a,r}$ itself does not provide sufficient information to determine local skin dose to a given patient. What is convenient about $K_{a,r}$ is that given proper geometrical information, it provides a free-in-air estimation of kerma which can be translated to the actual location of the patient's skin using a one-over-distance squared correction. When multiplied by a backscatter factor and the ratio of the mass energy absorption coefficients (MEAC) of skin to air, this value estimates the entrance surface dose, which at its highest value can be considered the peak skin dose (PSD). The relationship between $K_{a,r}$ and PSD forms the basis for skin dose mapping, whereby dose is "painted" onto a model of the patient's outer body contour.

Skin dose mapping can be implemented in real-time if exposure and geometric parameters are simultaneously made available to an external program for pairing with an anatomical patient model. In the past, there existed no mechanism for this type of implementation save a small number of programs which relied heavily upon proprietary access to extract information directly from the fluoroscopy unit.[8–11] The recent release of the DICOM radiation dose structured report (RDSR), however, has allowed for forthcoming widespread access to the type of information needed to describe the physical context of each irradiation event (An irradiation event describes a single depression of the fluoroscopy foot pedal). The RDSR functions as a digital storage file for parameters such as table and tube position, beam relevant parameters, and dose indicators such as $K_{a,r}$ and P_{KA}. It can be easily managed like other DICOM objects and accessed via an external DICOM compatible reader, of which there are several.[12,13] Currently, the RDSR can be manually exported during the procedure thus providing a mechanism for near real-time dose estimation. Alternatively, automatic export is provided at the end of the exam for postprocedure documentation. Future steps toward full automation and file streaming are included in the discussion section below.

To date, only one program has been developed which utilizes the RDSR to estimate peak skin dose. The system designed by researchers at the Mayo Clinic in Rochester, extracts geometric information from the RDSR and pairs this with a stylized reference phantom.[14] The system works by first determining the patient entrance reference point (PERP) using known distances. A four-sided projection pyramid is next conceptualized having its base at the PERP location and apex at the source location. The irradiated skin area is then determined according to mathematical equations which relate the four planes of the pyramid to points on the stylized phantom's surface. The skin dose mapping system has been installed within the Radiology Department at the Mayo Clinic and is presently undergoing validation and testing in a clinical setting.

The successful design and implementation of this program gives credibility to the type of skin dose mapping made available by the RDSR. In the present study, new software for calculating PSD from the RDSR is presented. The primary advantages are the incorporation of angular-dependent table and pad attenuation, the addition of MEAC ratios, the use of a flexible vector-based algorithm, and the implementation of more realistic outer body contours than those provided by stylized patient models. Additionally, a compelling case is made for the use of patient-sculpted phantoms based on the results of a patient-phantom matching study, whereby 26 patient-specific anatomical models were matched to phantoms using anthropometric measurement.

II. METHODS AND MATERIALS

II.A. RDSR extraction

Formally, the radiation dose structure report was created in 2005, with the release of Supplement 94 to the DICOM standard.[15] The RDSR thus represents a relatively new

Information Object Definition (IOD). The IOD is comprised of several DICOM attributes such as names, tags, and types, which are arranged according to specified Template IDentifiers (TID). The TIDs comprise a hierarchical tree structure where TID 10001 (Projection X-Ray Radiation Dose) contains TIDs 1002 (Observer Context), 10002 (Accumulated X-Ray Dose Data), and 10003 (Irradiation Event X-Ray Data). During an exam, there will be one instance of TID 1002 per procedure and up to two instances of TID 10002 depending on the fluoroscopy unit, either single or biplane. The number of exposures will determine the number of irradiation event templates.

Within each template are the attributes which help to describe the physical context of the irradiation. In order to access this information, a DICOM compatible reader is required. In this research, the programming language PYTHON was chosen along with the DICOM compatibility module Pydicom.[12,16] This selection was based on PYTHON's foundation as a general purpose, scientific-friendly programming language. Using the Pydicom module, a RDSR is read into a 2D array structure where each row is filled with the parameters corresponding to a single irradiation event. Table I lists these parameters. While the program fills the irradiation event array, it also simultaneously discriminates between planes A and B for biplane systems. Each of these planes is organized such that the data needed for dose reconstruction are made available.

II.B. Skin dose mapping algorithm

In order to translate the information extracted from the RDSR into PSD, a dose-mapping algorithm was constructed using programming tools available within MATLAB™. In this case, this matrix-based language provided the best option for code development. The final algorithm, however, was ported into PYTHON and compiled as an independent executable, later to be run directly within the interventional suite. The algorithm has several independent steps which are outlined in Secs. II B 1–II B 4.

TABLE I. Geometric and dose parameters extracted from the RDSR. These parameters are used by the skin dose mapping program to orient the tube with respect to the anthropomorphic model and to determine PSD.

RDSR Parameters
Table lateral position
Table longitudinal position
Table vertical position
Primary angle
Secondary angle
Source-to-detector distance
Source-to-isocenter distance
Peak tube voltage
Field of view
Air kerma at reference point
Air kerma-area product

II.B.1. Phantom formatting and orientation

In contrast to previous methods, the skin dose mapping software developed in this research is able to incorporate a variety of different phantom types. The only requirement is that the phantom be voxelized prior to use. The voxelization process allows for the 3D localization of the phantom's skin as a set of x, y, z coordinates, which correspond to the anterior/posterior, left/right, and superior/inferior directions. The voxel size is user selected and for this study was set at 5 mm. The process of phantom selection will be discussed at length in a later section.

For the purposes of design and testing, the skin dose mapping program was built around the specifications of the Siemens Artis Zee system installed within the Department of Radiology at Shands Jacksonville Medical Center. The Artis Zee system locates the C-arm isocenter at the table home position (0 cm lateral, 0 cm longitudinal, and 0 cm table height). Assuming a supine orientation with the tube located beneath the table, the posterior skin of the phantom correspondingly rests at the tube isocenter. For a prone orientation, the patient's anterior side would rest at isocenter. The position of the isocenter in relation to the head of the table is predetermined. The position of the patient's head in relation to the head of the table is then used to locate the phantom longitudinally. Additionally, the patient is assumed to lie in the middle of the table and a correction can be applied for any lateral displacement. Shifts in table height, latitudinal, and longitudinal positions as identified in the RDSR are directly applied to the phantom. The primary (LAO/RAO) and secondary (cranial/caudal) angles are then used in correspondence with the source-to-isocenter distance to determine the xyz location of the source in relation to the phantom.

II.B.2. Determination of affected skin area

Using the known positions of the phantom's skin in relation to the source, unit vectors are calculated from the origin and in the direction of each xyz skin location [see Fig. 1(a)]. The unit vectors are stored in a $[n \times 3]$ matrix. In order to determine which skin locations are found within the field of view, this matrix is rotated twice so as to orient the source-to-isocenter vector along a known axis [Fig. 1(b)]. Using the source-to-detector distance and FOV at the detector, two angles, α and β, needed to define a four-sided projection pyramid are calculated [Fig. 1(c)]. Two angles, γ and θ, are also calculated for each unit vector based on their relation to the chosen orientation axis [Fig. 1(d)]. By comparing these two angles with those calculated for the projection pyramid, a determination can be made as to which skin locations are found within the irradiated area.

A conditional statement culls the unit vectors based on their position either inside or outside the irradiation projection. To differentiate between skin locations on the entrance and exit sides of the phantom, the source-to-skin distance for each location determined to be within the beam is compared with minimum source-to-skin distance. A tolerance is set using this ratio and the FOV. The program then creates a list

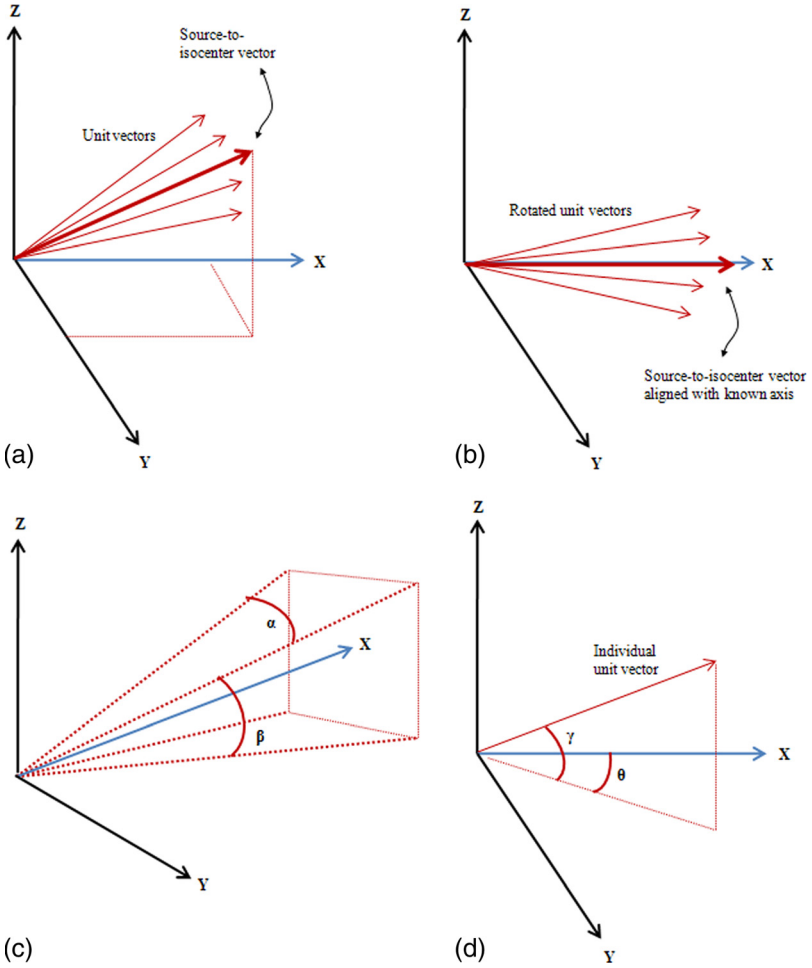

FIG. 1. Methodology for determining in-field skin locations: In Fig. 1(a), a unit vector from the source to each skin location is determined. In Fig. 1(b), these vectors are rotated such that they align with a known axis. In Fig 1(c), angles α and β are calculated from the FOV and source-to-detector distance and define a four-sided projection pyramid. In Fig 1(d), corresponding angles γ and θ are defined for each unit vector and compared to α and β within a conditional statement.

which includes the source-to-skin distance for each in-beam, entrance-side skin location.

II.B.3. Table attenuation

To account for table attenuation, the program calculates the distance through the table for each point found in the final list of affected skin locations. The distance is determined using each source-to-skin vector (unit vector multiplied by source-to-skin distance for each location) and the x, y, and z planes which describe the table location. By moving in small increments along the vector, the entrance and exit points can be established. The separation is then calculated directly as the distance between two points. Attenuation factors for the table material composition and density can be measured or selected from literature and applied to the dose algorithm.

II.B.4. Skin dose assessment

The calculation of dose is performed for each affected skin location according to Eq. (1) where BF is a backscatter factor selected from ICRU Report 74, $(\mu_{en}/\rho)_{skin}/(\mu_{en}/\rho)_{air}$ is the ratio of mass energy absorption coefficients for skin to air as determined from the NIST Physical Reference Data Library, and $e^{-\mu d}$ represents table attenuation.[17,18] The BF, MEAC ratio, and attenuation coefficient are energy dependent and chosen based on the effective energy of the x-ray beam. The BF is also field-size dependent. In contrast to the system developed by Khodadadegan *et al.*,[14] MEAC ratios for skin to air were included based on the understanding that these ratios vary between 0.92 and 0.97 within the diagnostic photon energy range. These ratios were calculated using mass energy absorption coefficients taken from the NIST library, where the elemental composition for skin was found in ICRP Publication 89.[19] These ratios were further validated through literature review (Ma and Seuntjens—Table II).[20]

In addition to these corrections, the RDSR has the capacity to store a clinically measured calibration factor to the reference point air kerma. In order to follow best practices, calibration should be performed to reduce uncertainty in this parameter below the FDA-recommended limit of $\pm 35\%$.[21] The calibration factor, CF, can then be applied directly for each irradiation event within the algorithm.

$$\text{Skin dose} = \text{Air kerma} \times \text{CF} \times \frac{\text{Dist to ref point}^2}{\text{Dist to skin location}^2} \times \text{BF} \times \left[\mu_{en}/\rho\right]_{\text{air}}^{\text{skin}} \times e^{-\mu d}. \quad (1)$$

Equation 1 is used to determine skin dose for each affected location for each irradiation event. The peak skin dose is then calculated as the maximum of these doses after the dose from each irradiation event has been summed at each

TABLE II. The skin dose mapping program determines the amount of skin area receiving doses within the four ranges where effects can be expected.

Single-Site Acute Skin-dose Range (Gy)	NCI Skin Reaction Grade	Approximate Time of Onset of Effects			
		Prompt	Early	Midterm	Long Term
0–2	NA	No observable effects expected	No observable effects expected	No observable effects expected	No observable effects expected
2–5	1	Transient erythema	Epilation	Recovery form hair loss	No observable effects expected
5–10	1–2	Transient erythema	Erythema, epilation	Recovery; at higher doses, prolonged erythema, permanent partial epilation	Recovery; at higher doses, dermal atrophy or induration
10–15	2–3	Transient erythema;	Erythema, epilation; possible dry or moist desquamation; recovery form desquamation	Prolonged erythema; permanent epilation	Telangiectasia; dermal atrophy or induration; skin likely to be weak
>15	3–4	Transient erythema; after very high doses, edema and acute ulceration; long term surgical intervention likely to be required	Erythema, epilation moist desquamation	Dermal atrophy secondary ulceration due to failure of moist desquamation to heal; surgical intervention likely to be required: at higher doses, dermal necrosis, surgical intervention likely to be required	Telangiectasia; dermal atrophy or induration; possible late skin breakdown; wound might be persistent and progess into a deeper lesion; surgical intervention likely to be required

skin location. In addition to PSD, the skin dose mapping program keeps track of the amount of skin area receiving doses within predefined dose levels. These levels are based upon a review on the effects of radiation on patient's skin and hair.[2] Table II lists the range of skin dose levels over which skin injuries are likely to occur, and has been reprinted here with permission from Dr. Balter.

II.C. Phantom selection

Over the past two years, the UF *Advanced Laboratory for Radiation Dosimetry Studies* (ALRADS) has developed the concept of hybrid phantoms and created a 50 member patient-dependent phantom library.[22,23] Patient-dependent phantoms increase patient specificity through the process of patient-phantom matching, whereby individuals are matched to different sized phantoms based on anthropometric measurement. In a previous study by the authors, patient-phantom matching was shown effective for increasing the accuracy of organ dose estimation for larger than average patients.[24] Organ size and location, however, played a large role in limiting the effectiveness for smaller than average patients. For skin dose mapping, the primary factor affecting dose is the calculation of the source-to-skin distance. In this case, even a slight change in a patient's body contour can lead to a different estimation of peak skin dose. Due to this fact, it was expected that patient-phantom matching would play a large role in reducing error for patients of all sizes.

In order to test this hypothesis, patient-phantom matching was investigated using five different phantom types including an elliptical reference phantom (40 cm wide/20 cm thick) representing the ORNL adult male, a 50th weight/height percentile reference hybrid phantom, a nearest weight/height percentile patient-dependent hybrid phantom, a CT image segmented patient-specific phantom, and a new measurement-based contour phantom. The concept of a contour phantom was based on the idea of creating a uniquely sculpted model for each patient. In order to create these phantoms at the time of examination, a stylized approach was necessary. In the future, automatic sculpting of the NURBS-based patient-dependent hybrid phantom can be pursued, thus allowing for rapid development of a unique surface phantom of the patient at the time of intervention.

For this work, contour phantoms were created for 26 patients (14 male/12 female). The surface of each contour phantom was defined according to three ellipse halves, one at each end and one in the middle. The ellipse halves themselves were defined by major and semiminor axes which were taken as measurements from each of 26 patient-specific phantoms. The patient-specific phantoms were created previously during the organ dose study by contouring CT datasets retrieved under IRB approval from the PACS system at Shands Jacksonville Medical Center.[24] The major axis represented the patient's lateral width, and the semiminor axis represented the patient's posterior/anterior width as measured for a supine patient. In total, six measurements were needed to create the phantoms and are illustrated in Fig. 2. It is feasible that the same six measurements could be taken prior to a fluoroscopy procedure by a radiology technician or nurse. The first ellipse halve would represent the patient's upper torso as measured near the top of the sternum, the second would represent the patient's middle torso as measured between the xiphoid process and naval, and the third would represent the patient's lower torso as measured near the middle of the sacrum. To actually construct each phantom, a MATLAB™ code was written which took as inputs each of the previously defined six measurements. The program begins

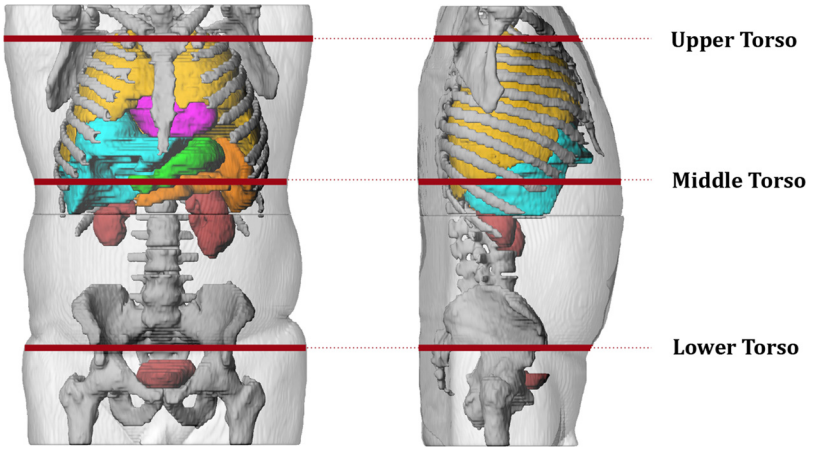

FIG. 2. Six measurements used to create patient-sculpted contour phantoms.

by defining the three ellipse halves and then interpolates between the three halves to complete the surface.

Patient-phantom matching was evaluated using six beam projections. The first set of three projections was centered on the heart and included tube rotations of 0, 90, and 180 degrees. The second set of projections was centered on the abdomen and also included tube rotations of 0°, 90°, and 180°. The image receptor field of view for all projections was set at 15×15 cm^2, the source-to-isocenter distance set at 72 cm, and the source-to-detector distance set at 100 cm. Peak-skin dose was calculated for each projection using each of the different phantom types. The process went as follows and was repeated for each patient (26 total as represented by 26 patient-specific phantoms – Fig. 3). First PSD was calculated for each projection using a patient-specific phantom. These values were used as the gold standard for comparison. Second, PSD was calculated using the reference stylized phantom. Third, the PSD was calculated using the reference hybrid phantom. Fourth, PSD was calculated using a patient-dependent phantom selected based on height and weight from the 25 male/25 female member UF patient-dependent hybrid phantom library. The selection process mirrored that followed in our previous organ dose study.[24] Finally, PSD was calculated using the uniquely created contour phantom which matched the patient as described previously. Accuracy was then quantified for each phantom type by calculating a percent-difference using the patient-specific dose as the true value. Figure 3 illustrates the different phantom types and matching technique.

II.D. Visualization

In order to provide 3D dose maps, the programming toolkit VTK is used to display skin dose at each affected location on the phantom surface.[25] A color map consisting of a blue to red spectrum indicates the intensity of the irradiated area. In order to highlight this component, several representative cases were processed. Skin dose maps were produced but are as yet not validated. The images are intended to illustrate the capabilities of the system and will be analyzed in a future publication focusing on dose reconstructions for specific cardiac and abdominal procedures.

III. RESULTS

Skin dose maps produced from seven test cases are shown in Fig. 4. In the image, dose has been painted onto the surface of seven different patient-dependent models. The figure emphasizes the effectiveness of the system for producing highly detailed dose maps, and also the ability to representing a diverse patient population. In Fig. 5, a comparison is made with a photograph of the actual patient [see review article Balter et al (Ref. 2)], whose exam parameters were used to produce the dose map. In all cases, the color maps are

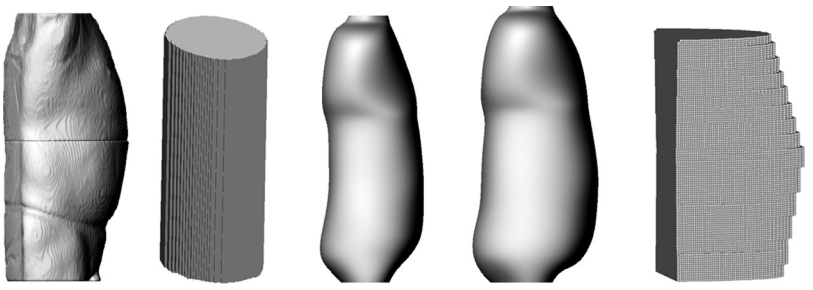

FIG. 3. For each patient-specific model, peak skin dose was also calculated for a reference stylized, reference hybrid, patient-dependent hybrid, and patient-sculpted contour phantom. Accuracy was quantified using the PSD calculated using the patient-specific model as the standard.

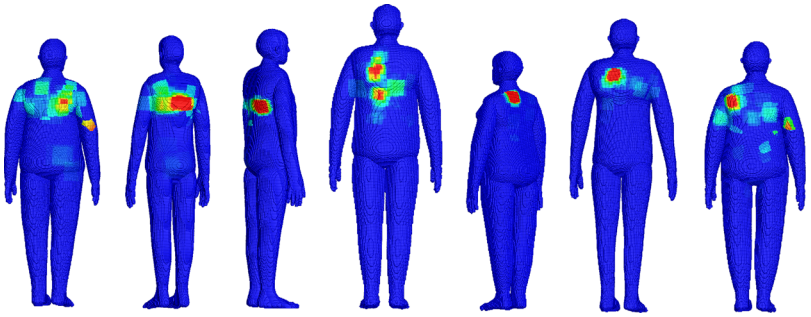

FIG. 4. Relative skin dose maps as calculated for seven patient exams. Skin doses are relative to the PSD for each individual patient.

relative to the cumulative postexamination PSD for each patient and are not given on an absolute dose scale.

The results for the patient-phantom matching study are highlighted in Table III. The table is organized by tube angle and gender, and lists percent difference between peak skin dose calculated using patient-specific phantoms and peak-skin dose calculated using stylized reference, hybrid reference, patient-dependent, and patient-sculpted phantoms, respectively. As in the previous patient-phantom matching study, the results have been aggregated according to patient size. The values found in the table represent the mean absolute percent difference for each group.

Several interesting trends were found. For posterior–-anterior projections, skin dose was seen relatively insensitive to anthropometric differences between the reference and patient-dependent phantom types. This follows the fact that for these projections, the source-to-skin distance is governed primarily by table height, not the patient contour. Another consideration is that for a supine patient, the posterior contour will flatten as a consequence of lying on a flat table. The patient-sculpted contour phantoms provided a completely flat posterior contour. This matched more closely with the posterior contour of the patient-specific phantoms, which were created directly from CT images. In a number of cases involving female patients, the patient-specific posterior contours were not completely flat due to an alternate patient positioning, where the torso was raised slightly above the table. For this reason, the mean difference for PA female projections was slightly higher than for males. In both cases, however, using a patient-sculpted contour phantom provided the most accurate dose estimates.

For left lateral projections, using a patient-dependent hybrid phantom had a small, but noticeable impact for both heavy and light patients. On average, the improvement was 2%–3% points better than using a hybrid reference phantom and 5%–10% points better than using a stylized reference phantom. For anterior–posterior projections, considerable improvement was seen when patient-phantom matching was employed to estimate the dose to large male patients. For females, using a patient-dependent phantom type also had a significant impact, in this case, most noticeably for abdominal projections for all patients and cardiac projections for light patients. The AP female projections were complicated by the large variability in patient and phantom breast sizing. Error in dose assessment was thus greatest for the AP female cardiac projections. Overall, the patient-sculpted contour phantoms again provided the most accurate dose estimates for all patients across both left lateral and AP projections, while the reference stylized phantoms provided the least accurate estimates by a wide margin.

IV. DISCUSSION

In terms of patient-phantom matching, the data found in Table III points toward two conclusions. First, error introduced by anthropometric differences is minimized for under the table projections. As mentioned above, this follows from the body flattening effects of the table and the fact that table height is the primary determinant of source-to-skin distance. Because the majority of fluoroscopic images are acquired using an under the table tube configuration, anthropometric differences are expected to introduce a very acceptable level of uncertainty in most situations.

Second, as the tube rotates to a more lateral position details about the patient contour become more important. In these cases, Table III indicates patient-sculpted phantoms provide the best means for estimating peak skin dose. While patient-dependent hybrid phantoms proved more effective than using a reference phantom for almost all left lateral and AP projections, the gains were roughly half of what was

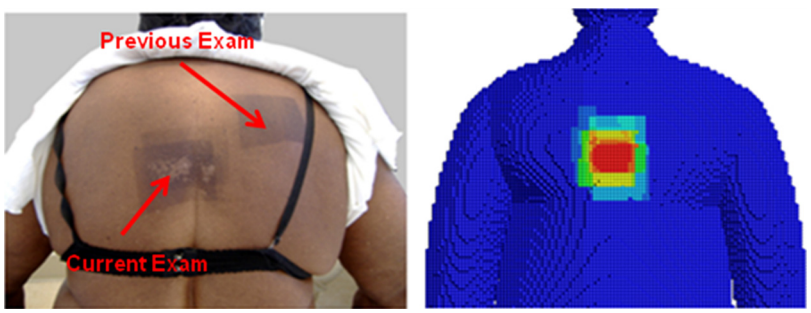

FIG. 5. Skin dose comparison between a real patient and anthropometrically matched hybrid patient dependent phantom (view is posterior). [Reprinted with permission from the Radiological Society of North America (RSNA). Balter, Hopewell, Miller, Wagner, and Zelefsky, "Fluoroscopically guided interventional procedures: A review of radiation effects on patients' skin and hair," Radiology **254**, 326-341 (2010)].

TABLE III. Mean absolute percent difference in PSD between patient-specific models and four different phantom types. Results are grouped according to patient size, tube projection, and orientation.

		Cardiac					Abdominal			
		Reference stylized	Reference hybrid	Patient-dependent	Patient-sculpted		Reference stylized	Reference hybrid	Patient-dependent	Patient-sculpted
Male						PA				
	Heavy	0.9	1.1	4.6	0.9		1.0	2.1	4.9	1.0
	Light	2.7	1.5	2.1	2.7		1.9	1.7	2.1	1.9
	All	2.0	1.4	3.0	2.0		1.6	1.8	3.1	1.6
						Lt Lat				
	Heavy	5.5	5.8	2.5	1.6		3.1	10.7	6.7	1.9
	Light	10.9	9.1	8.0	2.5		16.0	5.2	3.4	3.3
	All	9.0	7.9	6.0	2.2		11.4	7.1	4.5	2.8
						AP				
	Heavy	34.4	18.4	5.8	7.3		40.5	21.1	9.8	2.3
	Light	20.9	8.6	8.3	7.1		25.2	6.9	7.7	3.2
	All	25.7	12.0	7.4	7.2		30.6	12.0	8.4	2.9
Female						PA				
	Heavy	3.6	8.0	10.7	3.6		2.4	10.3	10.0	2.4
	Light	4.6	7.1	7.4	4.6		4.3	8.6	9.1	4.3
	All	4.2	7.5	8.7	4.2		3.5	9.3	9.5	3.5
						LT Lat				
	Heavy	9.2	13.3	12.1	5.5		12.4	19.1	14.5	5.5
	Light	11.6	5.5	3.0	3.9		19.7	4.5	6.3	3.8
	All	10.6	8.8	6.8	4.5		16.7	10.6	9.7	4.5
						AP				
	Heavy	39.1	8.6	9.8	5.2		46.7	22.4	9.1	9.0
	Light	16.8	29.1	17.1	9.8		16.2	20.3	11.3	6.3
	All	26.1	20.6	14.1	7.9		28.9	21.2	10.4	7.4

seen when using the patient-sculpted contour models. The ability to adapt to different patient thicknesses also provided a stark contrast between the stylized reference and patient-sculpted contour models, both of which were based on elliptical stylized surfaces. The fixed 20 cm thickness of the reference version led to large errors, which were significantly lessened when a sculpted phantom was used. On a case-by-case basis, the use of contour phantoms was most effective in situations where the anthropometric parameters of the patient-specific phantom lied outside the bounds of the current patient-dependent library. Also in cases, where the patient had a unique body type, contour phantoms provided significant improvements in comparison with hybrid phantoms.

The patient-sculpted models developed in this work represent a simple, but effective approach to patient contour modeling. By adding additional measurements, the specificity of these models could be improved. The primary factors to consider for building a better model are how any additional measurement would interrupt the workflow of the interventional suite, how different patient positioning of the arms and torso could be included, and how to better handle female specific issues related to breast sizing. The most important modeling aspect to keep in mind, however, is that the contour in contact with the table should be relatively flat.

Several other phantom options exist which fall under the various categories of patient-specific, patient-dependent, and patient-sculpted models. If individual CT data are available, a patient-specific outer-body contour phantom similar to those used in this study could be created. The primary limitation is the lack of CT imaging data for all patients. A further limitation is the added complexity of creating these phantoms in the clinic which would likely require strong physics support. Another option which falls under the patient-dependent category would be to investigate the use of the Civilian American and European Surface Anthropometry Resource (CAESAR) (Ref. 26) commercial database for providing patient outer body contours. This database contains 1D anthropometric measurements and 3D model scans of 2400 male and female subjects of ages between 18 and 65 years. The benefit of the CAESAR library is having a multitude of patient contours from which to choose. If the library could be automatically searched based on in-clinic anthropometric measurement, this may limit the need for patient-sculpting. The limitation again is the extra burden place on clinical staff to search this database and create phantoms for dose reconstruction. A final option is to use scripting tools within the modeling program RHINOCEROS™ (McNeel North America, Seattle, WA) to automate sculpting of hybrid phantoms. The final product would be a computational phantom with a set of organs with masses linked directly to reference vales and an outer body contour sculpted to match an individual patient. Such phantoms are already being designed at the UF ALRADS laboratory for organ dosimetry studies and the techniques for sculpting may prove useful for skin dose mapping if automation can be achieved.

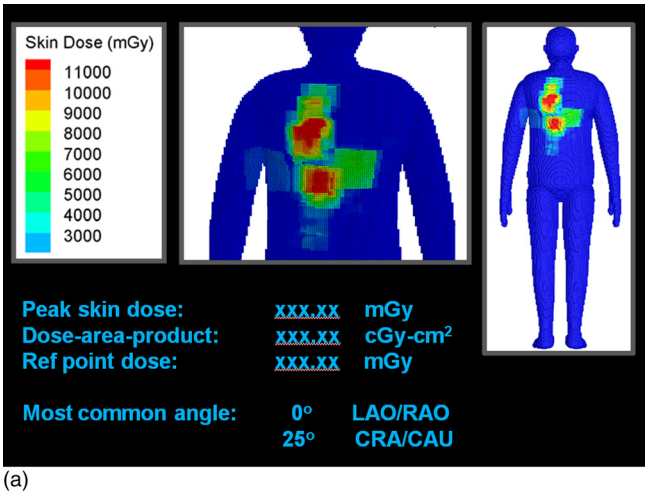

(a)

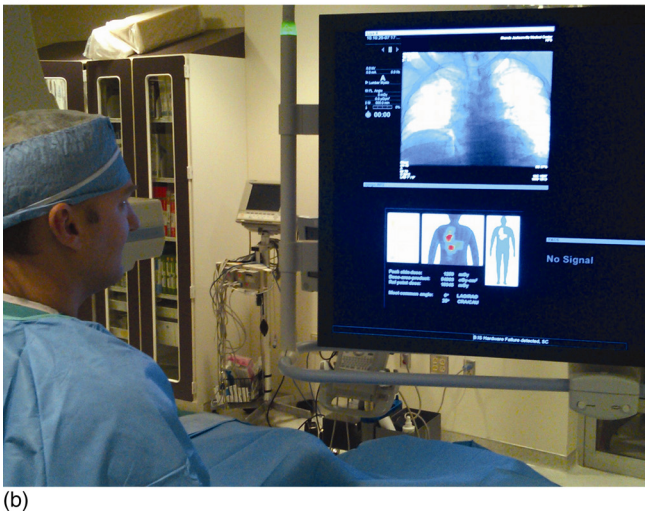

(b)

FIG. 6. (a) Prototype display of clinical skin dose mapping system. (b) Prototype display of dose map on the Siemens Artis Zee console. Co-author Dr. Dan Siragusa is shown in the left.

A secondary issue that arises from this study is how best to display the skin dose maps. In preparation for clinical implementation, a prototype display system was developed and placed on the in-clinic monitor of the Artis Zee system. The display is shown in Figs. 6(a) and 6(b). In the figure, a number of dose metrics are visible along with a hybrid-patient dependent model used to map skin dose. Additional features, including a system to warn the physician of substantial radiation dose levels (SDRL),[1] can be added based on recommendations made by the interventional physician. While contour models provide a higher level of accuracy, hybrid phantoms produce a more realistic looking anatomical figure. A future project will investigate the possibility of mapping a known dose distribution calculated from a contour model onto either a hybrid phantom or a similar animation-based model.

The work presented here and the skin dose mapping system by Khodadadegan *et al.*[14] share a number of disadvantages related to current limitations of the RDSR. Several of these were clearly outlined in the previous Mayo Clinic study, including the lack of collimator settings, an incomplete description of fluoroscopic panning, and issues related to the insertion of wedges and filters which have the potential to affect both $K_{a,r}$ and P_{KA}. One critical issue, not yet raised, is the lack of real-time data streaming. Initially, RDSRs were accessibly only at the close an exam. As a consequence, peak skin dose could not be calculated during the procedure or used to monitor patient risk. Streaming is already built into the IEC/DICOM specification, however, and recent updates to the Artis Zee system at Shands Jacksonville Medical Center have allowed for manual export of the RDSR during the interventional procedure. While this encouraging development provides a direct mechanism for in-procedure dose mapping, automated streaming is still unavailable at present. During correspondence with Heinz Blendinger, editor of Supplement 94, it was stated that *"The IHE REM (Radiation Exposure Monitoring) does not yet define an online dose reporting case, and also sending the full Dose SR for that purpose consecutive to each run may be seen as an overdriven solution."* However, it was also noted that "*Experiences from first implementations may help to refine this use case and derive requirements for maintaining changes to the DICOM Standard and potentially to the IHE REM profile.*"[27] From this statement, it is evident that the successful development and the implementation of dose monitoring systems will help to encourage the expansion of real-time reporting for the RDSR. In order to preliminarily test a real-time system, streaming can be simulated using time-stamps provided by the RDSR. In this way, the software can be optimized for real-time deployment. The current software system was designed with these thoughts in mind and is fully capable of rendering dose maps at a refresh rate of less than 1 s.

V. CONCLUSIONS

The purpose of the present study was to first introduce a new software system for determining peak skin dose, and second, to evaluate the effectiveness of patient-phantom matching on skin dose estimation. The skin dose mapping program operates by translating the reference point air kerma to the location of the patient's skin using geometric parameters extracted from the newly released Radiation Dose Structured Report. The patient surface is represented by a computational phantom defined as a set of points in three dimensional space. The program is nonproprietary and transferable and also functions independent to the software systems already installed on the control room workstations. The output is a three dimensional visual indication of localized skin dose which, once automated export or full streaming of the RDSR is available, can be used by the operating physician in near real-time to modify behavior when clinically appropriate.

Several different anatomical models were tested including reference stylized, reference hybrid, patient-dependent hybrid, and patient-sculpted contour phantoms. While patient-dependent hybrid phantoms provided better dose estimates than the hybrid and stylized reference phantom for lateral and anterior–posterior projections, the patient-sculpted contour phantoms were clearly superior at producing more accurate

skin dose estimates. These relatively simple models can be refined in future studies but are already accurate to within 1%–4% for PA projections, 2%–5% for left lateral projections, and 3%–8% for AP projections.

The primary drawback to the current system is the lack of real-time data streaming, although near real-time capabilities are presently possible. During upcoming clinical implementation, streaming will be tested using timestamps available within the RDSR. Assuming a real-time system, several other clinical aspects will also be investigated, including the clinical workflow, the automated monitoring of SDRLs, and the interaction of the interventionalist with the display system. Successful implementation of this system along with an increasing interest from the medical community as a result of NCRP Report No. 168 will help to encourage further progress in this area. The end goal is better patient care through the utilization of new technology.

ACKNOWLEDGMENTS

This work was support in part by Grant Nos.: RO1 CA116743 and CO6 CA059267 from the National Cancer Institute and Contract No.: HHS-N2612-0090-0098P from the NCI Radiation Epidemiology Branch.

[a]Author to whom correspondence should be addressed. Electronic mail: wbolch@ufl.edu; Telephone: (352) 846-1361; Fax: (352) 392-3380.

[1]NCRP, "Radiation dose management for fluoroscopically guided interventional medical procedures," NCRP Report No. 168 (National Council on Radiation Protection and Measurement, Bethesda, MD, 2010).
[2]S. Balter, J. W. Hopewell, D. L. Miller, L. K. Wagner, and M. J. Zelefsky, "Fluoroscopically guided interventional procedures: A review of radiation effects on patients' skin and hair," Radiology **254**, 326–341 (2010).
[3]The Joint Commission, "Sentinel event policies and procedures," http://www.jointcommission.org/Sentinel_Event_Policy_and_Procedures/ (2011).
[4]J. Anderson, G. Arbique, and J. Guild, "Peak skin dose reconstruction and TJC sentinel event [Abstract]," Med. Phys. **37**, 3373 (2010).
[5]A. Jones, "Risks in interventional radiology and establishing a patient safety program [Abstract]," Med. Phys. **37**, 3447 (2010).
[6]IEC, "Medical electrical equipment—Part 2-43: Particular requirements for the safety of x-ray equipment for interventional procedures," International Electrotechnical Commission 60601 (2000).
[7]FDA, "Federal performance standard for diagnostic x-ray systems and their major components—final rule," Fed Regist **70**, 33998–34042 (2005).
[8]K. Chugh, P. Dinu, D. R. Bednarek, D. Wobschall, S. Rudin, and K. Hoffmann, "A computer-graphic display for real-time operator feedback during interventional x-ray procedures," Proc SPIE **5367**, 464–473 (2004).
[9]A. den Boer, P. J. de Feijter, P. W. Serruys, and J. R. T. C. Roelandt, "Real-time quantification and display of skin radiation during coronary angiography and intervention," Circulation **104**, 1779–1784 (2001).
[10]N. A. Gkanatsios, W. Huda, K. R. Peters, and J. A. Freeman, "Evaluation of an on-line patient exposure meter in neuroradiology," Radiology **203**, 837–842 (1997).
[11]S. Balter, "Methods for measuring fluoroscopic skin dose," Pediatr Radiol. **36** (Suppl 2), 136–140 (2006).
[12]Pydicom, http://code.google.com/p/pydicom/ (2011).
[13]OFFIS, http://dicom.offis.de/software.php.en (2011).
[14]Y. Khodadadegan, M. Zhang, W. Pavlicek, R. G. Paden, B. Chong, B. A. Schueler, K. A. Fetterly, S. G. Langer, and T. Wu, "Automatic monitoring of localized skin dose with fluoroscopic and interventional procedures," J Digit. Imaging **24**, 626–639 (2010).
[15]DICOM Standards Committee Working Group 6, *Supplement 94: Diagnostic x-ray radiation dose reporting (Dose SR)* (Rosslyn, Virginia, 2005).
[16]Python, http://www.nist.gov/pml/data/xraycoef/index.cfm (2011).
[17]ICRU, "ICRU Report 74: Patient dosimetry for x-rays used in medical imaging," J. ICRU **5**, 1–50 (2005).
[18]J. Hubbell and S. Seltzer, "Tables of x-ray mass attenuation coefficients and mass energy-absorption coefficients (Version 1.4) [Online]," http://physics.nist.gov/zaamdi.
[19]ICRP, "ICRP Publication 89: Basic anatomical and physiological data for use in radiological protection—reference values," Ann ICRP **32**, 1–277 (2002).
[20]C. M. Ma and J. P. Seuntjens, "Mass-energy absorption coefficient and backscatter factor ratios for kilovoltage x-ray beams," Phys. Med. Biol. **44**, 131–143 (1999).
[21]B. Schueler, "Patient dose and the modern angiographic system [Abstract]," Med. Dosim. **37**, 3335 (2010).
[22]C. Lee, D. Lodwick, J. Hurtado, D. Pafundi, J. L. Williams, and W. E. Bolch, "The UF family of reference hybrid phantoms for computational radiation dosimetry," Phys. Med. Biol. **55**, 339–363 (2010).
[23]P. Johnson, S. Whalen, M. Wayson, B. Juneja, C. Lee, and W. Bolch, "Hybrid patient-dependent phantoms covering statistical distributions of body morphometry in the US adult and pediatric population," Proc. IEEE **97**, 2060–2075 (2009).
[24]P. B. Johnson, A. Geyer, D. Borrego, K. Ficarrotta, K. Johnson, and W. E. Bolch, "The impact of anthropometric patient-phantom matching on organ dose: A hybrid phantom study for fluoroscopy guided interventions," Med. Phys. **38**, 1008–1017 (2011).
[25]VTK, "Visualization tool kit," http://www.vtk.org/ (2011).
[26]http://store.sae.org/caesar/.
[27]H. Blendinger, Siemens AG (Personal correspondence, 2009).